# Supplementary Material

## Photonic-Enhanced Perovskite Solar Cells: Tailoring Colour and Light Capture

Eva Almeida[1], Miguel Alexandre[1], Ivan M. Santos[1],
Rodrigo Martins[1], Hugo Águas[1*], Manuel J. Mendes[1*]

[1]i3N/CENIMAT, Department of Materials Science, NOVA School of Science and Technology and CEMOP/UNINOVA, Monte da Caparica, 2829-516, Caparica, Portugal.


*Corresponding author(s). E-mail(s): hma@fct.unl.pt;
mj.mendes@fct.unl.pt;
Contributing authors: e.almeida@campus.fct.unl.pt;
m.alexandre@campus.fct.unl.pt; imi.santos@campus.fct.unl.pt;
rfpm@fct.unl.pt;

# S1 FDTD setup

This section provides further detail on the setup of the Finite Difference Time Domain (FDTD) solver, namely the implementation of non-linear material data and the spatial/temporal simulation conditions.

The 3D FDTD unit cells of the various configurations are illustrated in Figure 1(b)–(f), from an $xy$ plane view, and incorporate all the layers seen in Figure 1(a), in the $z$ direction. Since the structures from this study are composed of arrays with symmetry in $x$ and $y$ (with the exception of linear gratings), it was possible to select periodic symmetric and antisymmetric boundary conditions in these axes, respectively, thus reducing the simulation time to a quarter. In the $z$ axis, the bottom boundary was designated as metal, since the last planar layer of the device, composed of gold, is highly reflective. Lastly, the top $z$ boundary was defined as a combination of Perfectly Matched Layers (PML), responsible for the absorption of any incident energy and for impedance matching to the surrounding material, to nullify the reflection in the unit cell limits. The application of these periodic boundary conditions in the FDTD region enabled the implementation of a single-polarized planar wave source (P-polarized, by default), to minimize the computational time of the simulations.

Since 1D grating lines do not uphold the aforementioned array symmetry, the simulation of these structures was performed under two source polarizations, P and S. In this case, the values of the unpolarized $J_{SC}$ and the reflection spectra were obtained by calculating the average of the respective quantities of both polarizations.

By the nature of the FDTD algorithm, the discretization in space is directly defined by the simulation mesh. By default, the FDTD region has a non-uniform global mesh, to which an accuracy value can be attributed. By increasing the global accuracy, the mesh spacing decreases, at the expense of computational memory and time. However, when studying complex designs, such as the light-trapping structures of this work, it is advised to implement additional meshes in regions where the electric and magnetic fields ought to vary drastically. Figure S1 exhibits a side-view of the solar cell layers, as well as the two additional meshes implemented in the model: the top mesh, which includes the photonic structures, the ITO and $SnO_2$ planar layers and the top 100 nm of the perovskite layer; the bottom mesh, that covers the bottom 100 nm of the perovskite layer and the top 50 nm of the Spiro layer. These meshes increase the accuracy of the optical estimations in these regions, where the main interfaces were included, to avoid numerical errors associated to the sudden change of the fields.

The main settings of the aforementioned FDTD objects were selected after conducting a series of convergence tests, further analysed in Section S1.1. These were applied when simulating solar cells under a planar light source, at a normal angle with the surface.

Simulating solar cells with illumination at oblique angles required different boundary conditions and mesh definitions. When applying a plane wave source at an angle (defined as $\theta$), the symmetry in periodicity can no longer be assumed. For this reason, Bloch boundary conditions were selected for the unit cell, to account for the fields phase changes across each period. Additionally, the optical results of these simulations are no longer identical for all polarization angles, despite the layout symmetry. Thus, it was necessary to calculate the average results between two different light
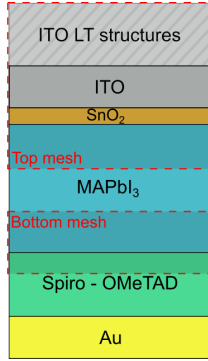
**Fig. S1** Layout of the planar configuration of the perovskite solar cells and placement of the LT structures, along with the additional meshes inserted in the FDTD region: top mesh(cover the LT, ITO, SnO$_2$ and the top 100 nm of the perovskite layer) and bottom mesh (covers the bottom 100 nm of the perovskite and top 50 nm of the Spiro layer).

polarizations (P-polarized — considered a 0° polarization angle, and S-polarized — considered a 90° angle). The settings were adapted for these conditions in another set of convergence tests, as disclosed in Section S1.2.

## S1.1 Convergence testing: normal-incident illumination

In order to increase the computational efficiency of the optical simulations, carried out by the Lumerical software, a range of mesh and unit cell boundary definitions were tested. Regarding the accuracy of the simulation space, the following three aspects were accounted for:

- Additional mesh regions: the mesh spacing can be modulated by defining an equivalent index of certain regions: as this index increases, the mesh becomes more compact, and the accuracy of the results enhances, at the expense of simulation time. The equivalent indices of the top and bottom meshes (previously described in Section S1, Figure S1) were tested between $(x, y, z) = (3, 3, 3)$ and $(x, y, z) = (5, 5, 5)$, with a step of $1/6$.
- FDTD region mesh: the accuracy of the global simulation region mesh was varied between 2 (fast simulation, low accuracy) and 4 (good tradeoff between accuracy and memory)
- Number of PMLs: the increase of the amount of PML layers decreases the reflection at the limits of the FDTD region, avoiding resonance derived artifacts in the results. This parameter was increased when necessary, to guarantee that the simulation triggered the autoshutoff feature in the FDTD solver.

To minimize computational time while preserving the accuracy of the results, a variety of combinations of the previous FDTD parameters were tested. Their impacts on the current density were obtained for solar cells with crossed gratings (top graphs of Figure S2) and domes (bottom graphs of Figure S2), for the previously itemized ranges of equivalent mesh index and global accuracy. These 2D plots exhibit the $J_{SC}$ values

which, ideally, should not be influenced by the simulation settings. Thus, the best FDTD parameters correspond to the areas of the plots where $J_{SC}$ stabilizes around a plausible value.

The amount of PML layers was set to 16 for every structure (relatively high value, since the geometry of the simulation objects is somewhat complex), except for the solar cells with linear gratings, where it was necessary to increase this number to 32, in order for the system to reach autoshutoff.

The settings obtained for crossed gratings were applied to linear gratings and checkerboards, while the dome parameters were used for the nanopillars. The selected configurations are summarized in Table S1.
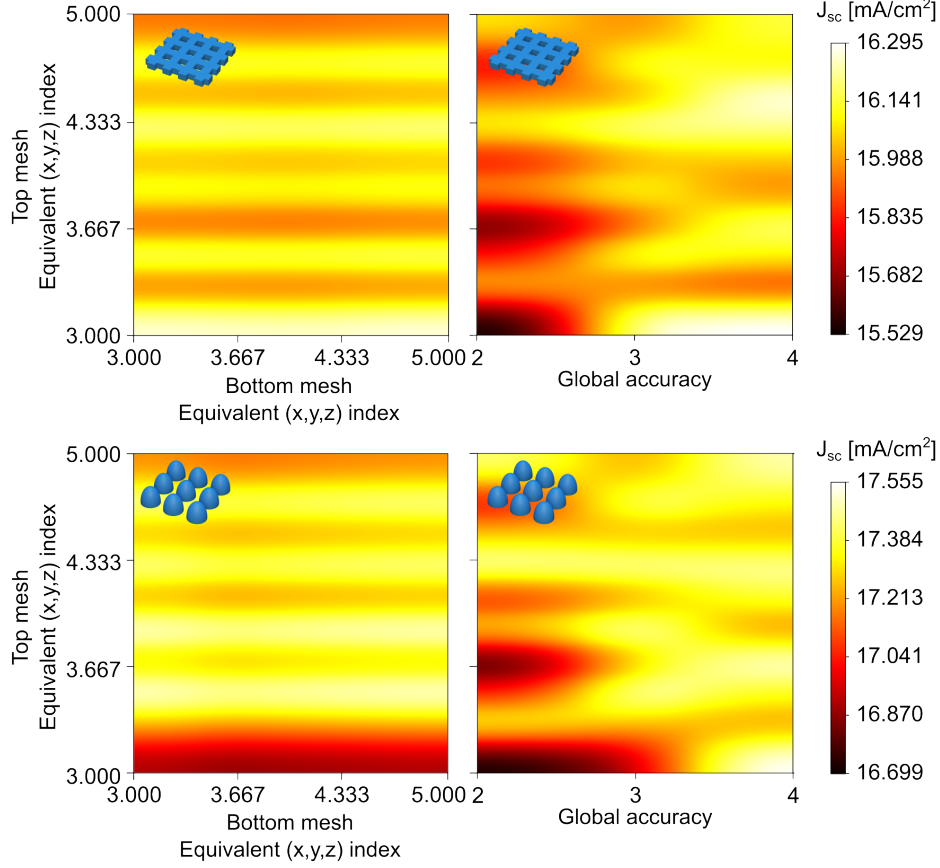


**Fig. S2** Convergence analysis for FDTD simulations: $J_{SC}$ for different values of the FDTD setup parameters, equivalent mesh index of the additional meshes (referred as top and bottom meshes) and global region mesh accuracy. The top graphs indicate the results obtained for solar cells with crossed gratings, while the bottom row corresponds to the solar cells with domes.

**Table S1** FDTD mesh and boundary condition settings used for the simulations of solar cells with photonic structures. The parameters were selected from the results of the convergence tests detailed in Figure S2, consisting of the accuracy of the global region mesh, the equivalent indices of the additional meshes (referred as top and bottom meshes) and the amount of PML layers.

| Structures | Top mesh Equivalent Index $(x, y, z)$ | Bottom mesh Equivalent Index $(x, y, z)$ | Global accuracy | Number of PML |
|---|---|---|---|---|
| Linear Gratings | $(4.333, 4.333, 4.333)$ | $(3, 3, 3)$ | 3 | 32 |
| Crossed Gratings | $(4.333, 4.333, 4.333)$ | $(3, 3, 3)$ | 3 | 16 |
| Checkerboards | $(4.333, 4.333, 4.333)$ | $(3, 3, 3)$ | 3 | 16 |
| Circular nanopillars | $(4.333, 4.333, 4.333)$ | $(3, 3, 3)$ | 3 | 16 |
| Domes | $(4.333, 4.333, 4.333)$ | $(3, 3, 3)$ | 3 | 16 |

## S1.2 Convergence testing: oblique illumination

The FDTD setup for the simulation of solar cells under oblique illumination angles ($\theta$ ranged between 0° and 60°) was defined and validated by a separate set of convergence tests. For these conditions, the absorption in the perovskite layer of the planar configuration of the solar cells was compared to the results of an analytical approach — the scattering matrix method — as seen in Figure S3. The aforementioned FDTD settings (from Table S1) were tested for 0°, 30° and 60°, and the absorption spectra were attained for P-polarized (TE) and S-polarized (TM) light sources. The best results were obtained for a top mesh index of 4.5 and 32 layers of steep-angle PML, with which the numerical simulation of the planar cells showed identical spectra to the results acquired by the analytical method.
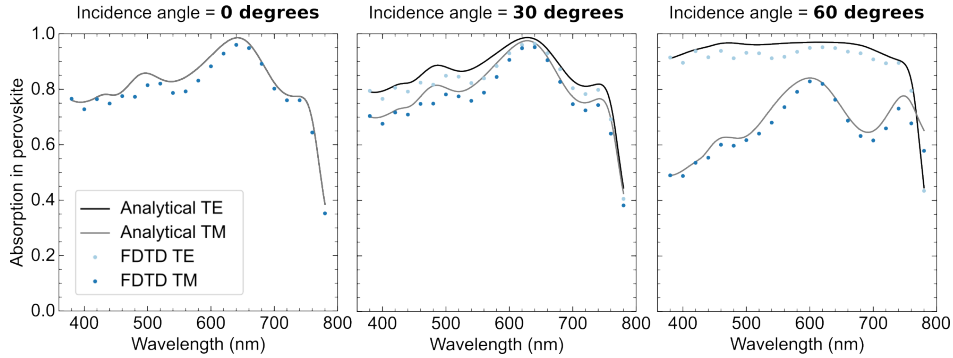


**Fig. S3** Comparison between the perovskite absorption spectra obtained by the FDTD simulations, in Lumerical, with the spectra attained by the scattering matrix analytical method, for P-polarized (TE) and S-polarized (TM) light sources.

## S1.3 Material data

The spectra of the refractive indices and extinction coefficients of the materials implemented in the FDTD model of the solar cells are shown in Figure S4. The fit of these curves performed by the software is presented as well.
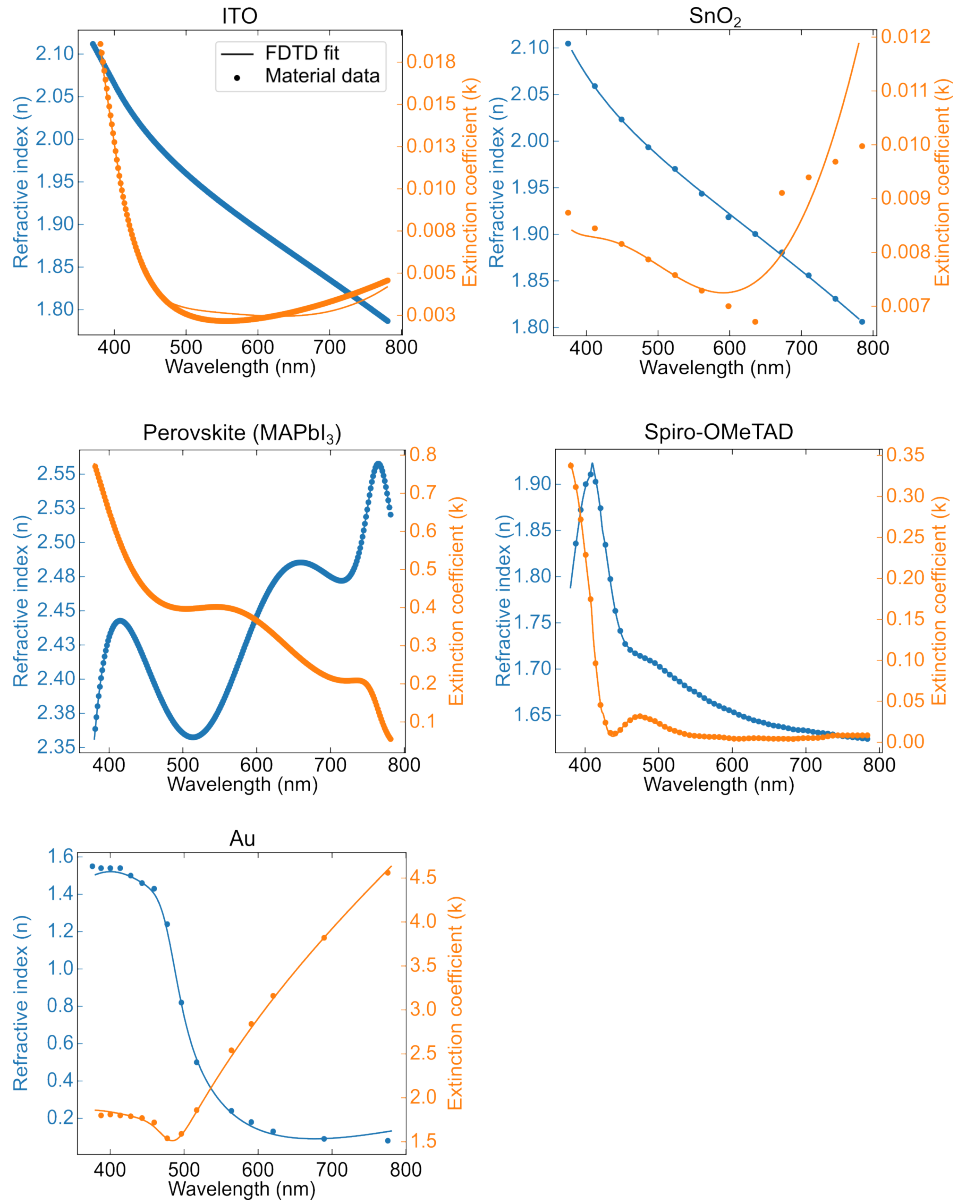


**Fig. S4** Real ($n$) and imaginary ($k$) components of the refractive index of the materials adopted in the simulations of the solar cells depicted in Figure 1(a). The data was obtained from [1].

# S2 Screening of shape and array symmetry

Since the light trapping structures hold so much weight on the outward scattering, reflection and refraction angles and consequent constructive interference of the light reflected by the cell, it is interesting to observe the effect of their shape and array symmetry in the final cell chromaticity

To this end, two different pillar shapes were compared, circular and squared. The chromaticity of these two cells is present in Figure S5, for different combinations of dimensional parameters: pitch, height and radius/width. It is clear, by the similarity of the results obtained for both shapes, that the particular shape of the nanopillars does not hold much influence on the cell colour. Therefore, the optimization of both structures was deemed unnecessary, since the results are identical. As circular pillars present radial symmetry (ensuring simulation accuracy with the symmetric/anti-symmetric boundary conditions applied to the FDTD region), this shape was considered for optimization in this work, alternatively to the squares.
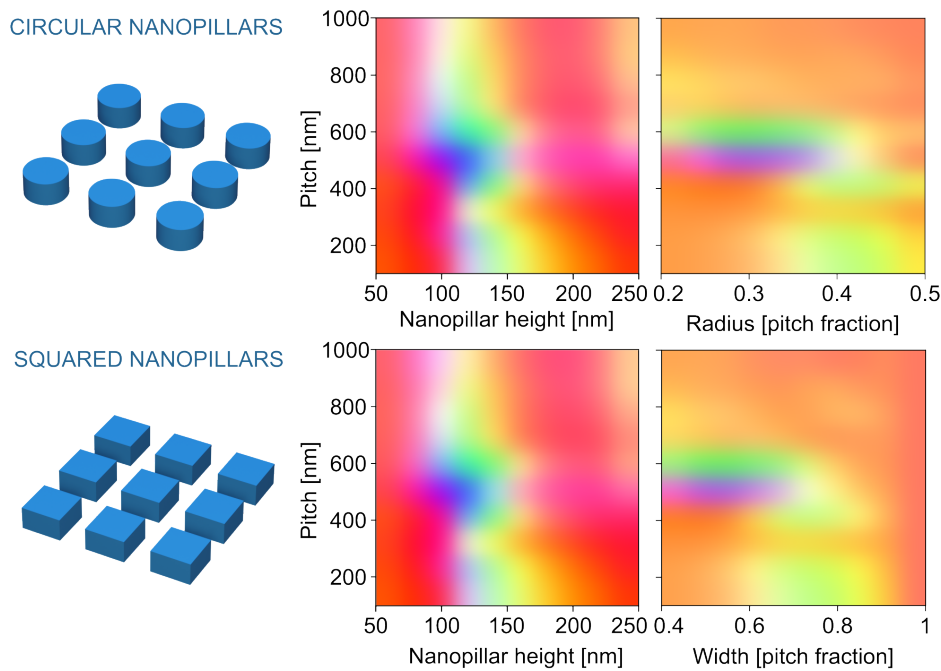


**Fig. S5** Chromaticity of solar cells with circular (top graphs) and squared (bottom plots) nanopillars, for various combinations of photonic structure dimensioning of the parameters pitch, height and radius/width.

Analogously, the circular nanopillars and domes were studied in different array symmetries, square (illustrated in Figure S6(b) and S6(d)) and hexagonal (Figure S6(a) and S6(c)). The corresponding chromaticity and current density for different sized cells can be seen in the graphs of Figure S6. For a finer comparison,

the ratio of the unit cell area that is occupied by the photonic structures was varied, by changing the features' radii while maintaining a fixed pitch. Figure S6 reveals that the chromaticity of cells with circular nanopillars showed few differences between symmetries. Contrarily, the solar cells with domes resulted in notable colour disparities. With respect to $J_{SC}$, the hexagonal array symmetry outperformed the square array, as formerly concluded by many studies [2–4]. Despite the slight improvement of the results obtained by hexagonal symmetry, these were regarded as negligible, since the magnitude of colours attained for each structure is similar, as well as the $J_{SC}$ ranges. Consequently, these structures were optimized in square array symmetry, since a smaller unit cell reduces simulation time.
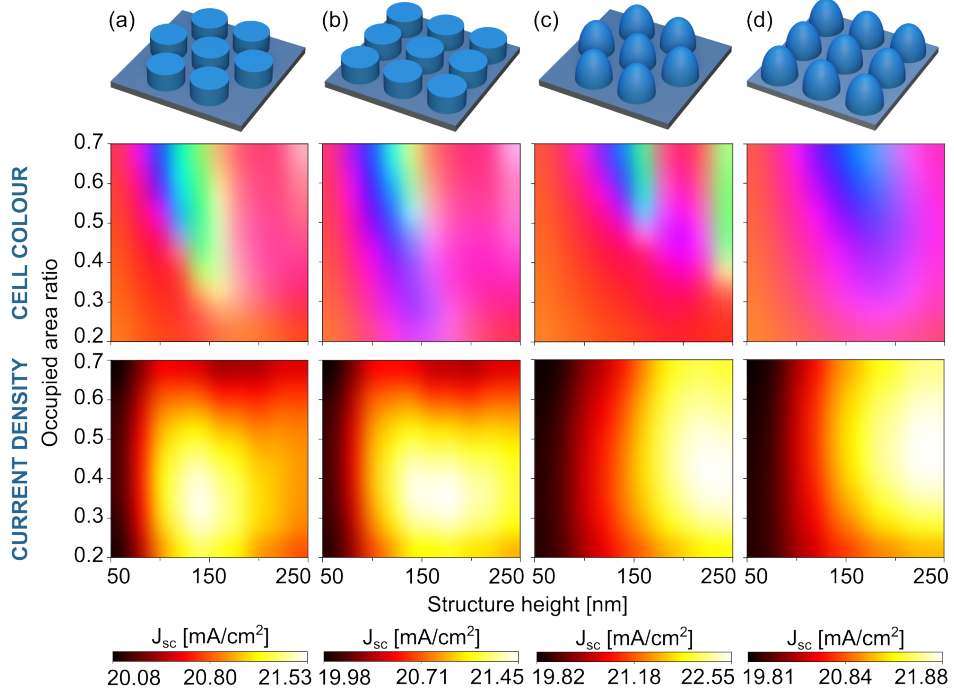


**Fig. S6** Chromaticity and current density for a variety of combinations of dimensional parameters (structure heights and area ratios occupied by the photonic structures), for different array layouts of (a), (b) circular nanopillars and (c), (d) domes: (a), (c) hexagonal and (b), (d) square symmetries.

On another note, the sweep of the width/radius of the solar cells, as represented in Figure 4 of main text, was performed for the remaining structures (domes and linear gratings). The corresponding chromaticity and current density spectra attained for all types of investigated features are displayed in Figure S7. Their analysis is present in the main article, in Section 2.2.
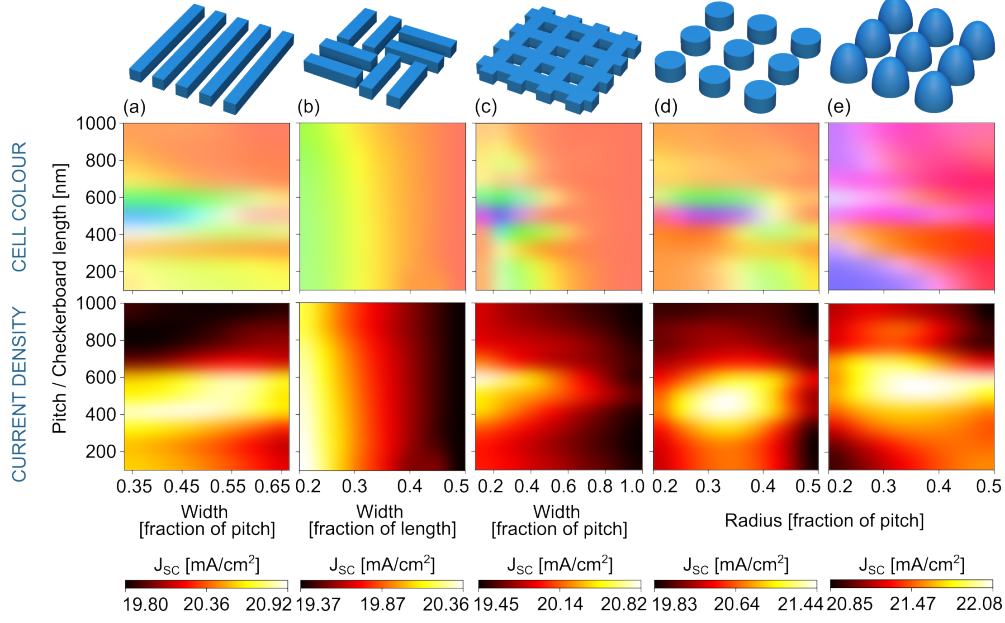
**Fig. S7** Chromaticity (top plots) and photocurrent density (bottom plots) spectra for different combinations of pitch and width/radius (structure height fixed at 100 nm and Z radius at 400 nm) for a variety of LT structures: (a) linear gratings, (b) checkerboards, (c) crossed gratings, (d) circular nanopillars and (e) domes in square symmetry.

## S3 Definition of the Figure of Merit

The Figure of Merit developed for this work was selected among a series of expressions, represented in Equations (S1) to (S4), to be maximized by an optimization algorithm. These functions have the same variables with slight deviations. $FoM_1$, $FoM_2$ and $FoM_3$ include the parameter "colour limit", which introduces the concept of the human eye sensitivity, by approaching a certain range of RGBs as sufficiently close to the optimal colour. As discussed in the main article, this value was set to 15: when the RGB of the solar cell is at a small euclidean distance from the optimal value (lower than 15), the search space is entirely defined by the $J_{SC}$. On the other hand, $FoM_0$ does not incorporate this parameter, forcing the algorithm to search for a specific RGB value, disregarding cell configurations with similar colour and higher optical performance. The remaining functions are identical, defined solely to test different root values under the condition of RGB distance > Colour limit.

$$\text{FoM}_0 = \begin{cases} J_{sc} & \text{RGB distance} = 0 \\ \dfrac{J_{sc}}{\sqrt{\text{RGB distance}}} & \text{RGB distance} > 0 \end{cases} \tag{S1}$$

$$\text{FoM}_1 = \begin{cases} J_{sc} & \text{RGB distance} \leq \text{Colour limit} \\ J_{sc} \times \dfrac{\text{Colour limit}}{\text{RGB distance}} & \text{RGB distance} > \text{Colour limit} \end{cases} \tag{S2}$$

$$\text{FoM}_2 = \begin{cases} J_{sc} & \text{RGB distance} \leq \text{Colour limit} \\ J_{sc} \times \sqrt{\dfrac{\text{Colour limit}}{\text{RGB distance}}} & \text{RGB distance} > \text{Colour limit} \end{cases} \tag{S3}$$

$$\text{FoM}_3 = \begin{cases} J_{sc} & \text{RGB distance} \leq \text{Colour limit} \\ J_{sc} \times \sqrt[3]{\dfrac{\text{Colour limit}}{\text{RGB distance}}} & \text{RGB distance} > \text{Colour limit} \end{cases} \tag{S4}$$

Figure S8 shows the search space defined by Equations (S1) to (S4), in a range of geometrical parameters (different values of grating height and pitch), obtained for P-polarized simulations of the solar cells with linear gratings. The purpose of visualizing the search space is to observe how the FoM advances towards the maxima, thus evaluating the mobility freedom of the PSO "particles" (parameter sets). Ideally, the peaks should be broad, as to facilitate the search and to guide the PSO particles towards the top. The $\text{FoM}_0$ function behaviour, seen in Figure S8, shows highly-defined and isolated peaks, that are challenging to find during the optimization. Therefore, $\text{FoM}_0$ is not proper for this work, since the RGB aspect holds too much merit in the function. By introducing the colour limit to the expression, $\text{FoM}_1$ shows some improvements, as the peaks start to expand. By increasing the root value, from $\text{FoM}_1$ to $\text{FoM}_3$, the weight of the RGB distance reduces in the function, broadening the maxima peaks and improving the particles mobility in the seach space. As the function layouts of $\text{FoM}_2$ and $\text{FoM}_3$ were identical, $\text{FoM}_2$ was chosen for the solar cell optimizations in this work, to minimize the complexity of the method.

To further analyse the behaviour of these functions, two PSOs were performed, to compare the reference function, $\text{FoM}_0$, to the selected alternative, $\text{FoM}_2$. By fixing the initial characteristics of the particles, it was possible to partially remove the stochastic aspect of the process, thus exposing how the functions progress. This test was performed on solar cells with linear gratings (P-polarized) and the results are visible in Figure S9, where each scatter point represents the position of one particle, in the corresponding cell colour. A simple analysis of these results points to the advantages of $\text{FoM}_2$, namely higher optimal $J_{\text{SC}}$ and higher FoM values for near-magenta configurations.
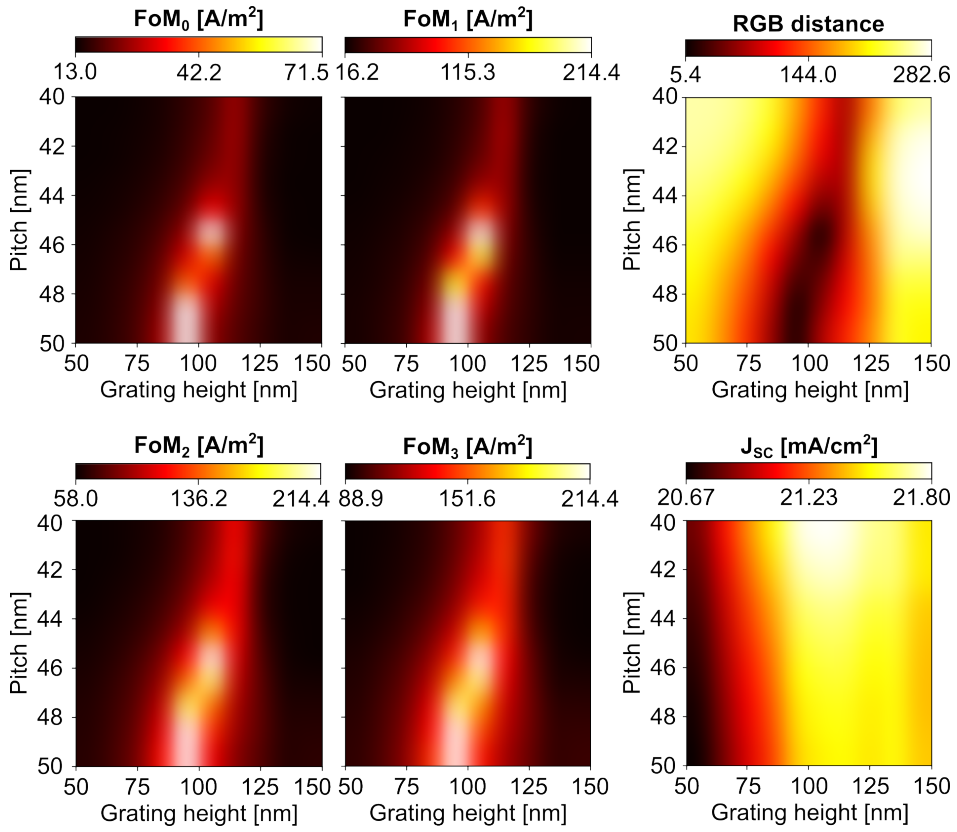
**Fig. S8** Search space defined by Equations (S1) to (S4), corresponding respectively to FoM$_0$ to FoM$_3$, for different combinations of pitch and gratings height of P-polarized magenta solar cells with linear grating structures. The function variables, colour distance and $J_{SC}$, are also portrayed. When necessary, the colour limit was set to 15.
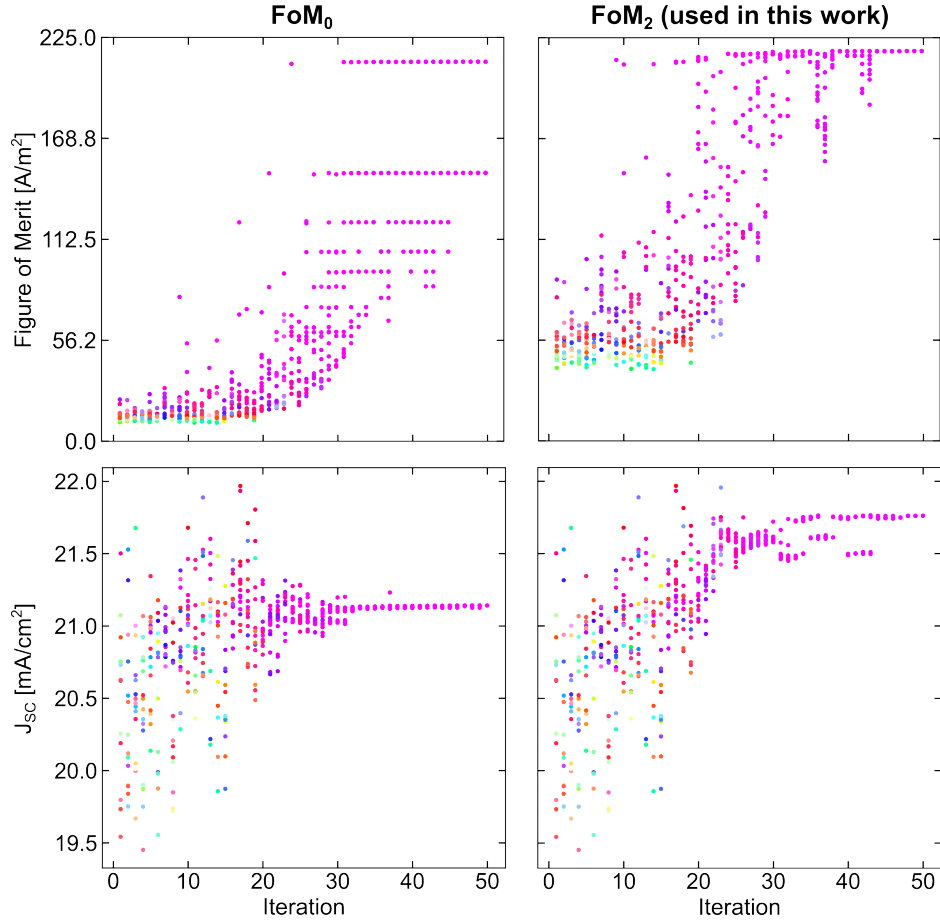
S11

**Fig. S9** Progress of FoM (top plots) and $J_{SC}$ (bottom plots) values for 15 particles (parameter sets) during the optimization of magenta solar cells with linear grating (P-polarized). The initial seeds of the particles were fixed for both PSO processes, for an adequate comparison of the progression of $FoM_0$ (left column) and $FoM_2$ (right column, for a colour limit of 15). Each scatter point represents the position of one particle and the corresponding cell colour.

# S4 Particle Swarm Optimization: setup and results

After extensive preliminary simulations and parameters assessments, the variable ranges were defined and inserted in the optimization algorithm of the solar cell geometry. These are exhibited in Table S2. To avoid extreme size aspect ratios, the height of the domes was restricted between radius $\leq$ Z radius $\leq 2 \times$ radius. Despite refraining from manufacturing complications and irregularities, these constraints might interfere in the trajectory of the PSO particles, due to variable interdependencies and limitations. Regarding the PSO specifications, 25 particles navigated the search space, for 50 iterations, the inertia weight constant varied from 0.9 to 0.4 and the cognitive and the social coefficients were both set to 1.45.

**Table S2** Variable ranges [bottom limit, top limit] used in the optimization of planar and photonic-structured solar cells, for magenta and green.

| Variables | Planar | Linear gratings | Checkerboards | Crossed gratings | Circular nanopillars | Domes |
|---|---|---|---|---|---|---|
| Pitch (nm) | NA | $[100, 1000]$ | $[200, 2000]$ | $[100, 1000]$ | $[100, 1000]$ | $[250, 1000]$ |
| Width/Radius (pitch fraction) | NA | $\left[\dfrac{1}{3}, \dfrac{2}{3}\right]$ | $[0.10, 0.25]$ | $\left[\dfrac{1}{3}, \dfrac{2}{3}\right]$ | $[0.2, 0.5]$ | $[0.2, 0.5]$ |
| Structure height (nm) | NA | $[50, 250]$ | $[50, 250]$ | $[50, 250]$ | $[50, 250]$ | $[50, 1000]$ |
| ITO thickness (nm) | $[50, 250]$ | $[50, 250]$ | $[50, 250]$ | $[50, 250]$ | $[50, 250]$ | $[50, 250]$ |
| Spiro thickness (nm) | $[100, 200]$ | $[100, 200]$ | $[100, 200]$ | $[100, 200]$ | $[100, 200]$ | $[100, 200]$ |

The particle swarm algorithm is a population smart-search method based on stochastic and metaheuristic solutions. Due to these aspects, the optimization is likely to return local maxima of the FoM, instead of the global maximum, since the search space is rather complex and vast. To prevent this, multiple PSOs were performed for wide variable amplitudes. It was found that the optimal parameters were frequently agglomerated around similar values, which enabled the narrowing of the variable ranges, for which supplementary PSOs were performed. The optimal geometrical parameters of all these PSOs are present in Figures S10 to S15, represented by circular (wide-ranged) and star shaped (narrow-ranged) markers, along with the corresponding FoM, $J_{SC}$ and RGB distance values.

The top results of the PSOs previously referred are present in Table S4 and the corresponding optimal geometries are mentioned and illustrated in Table S3.
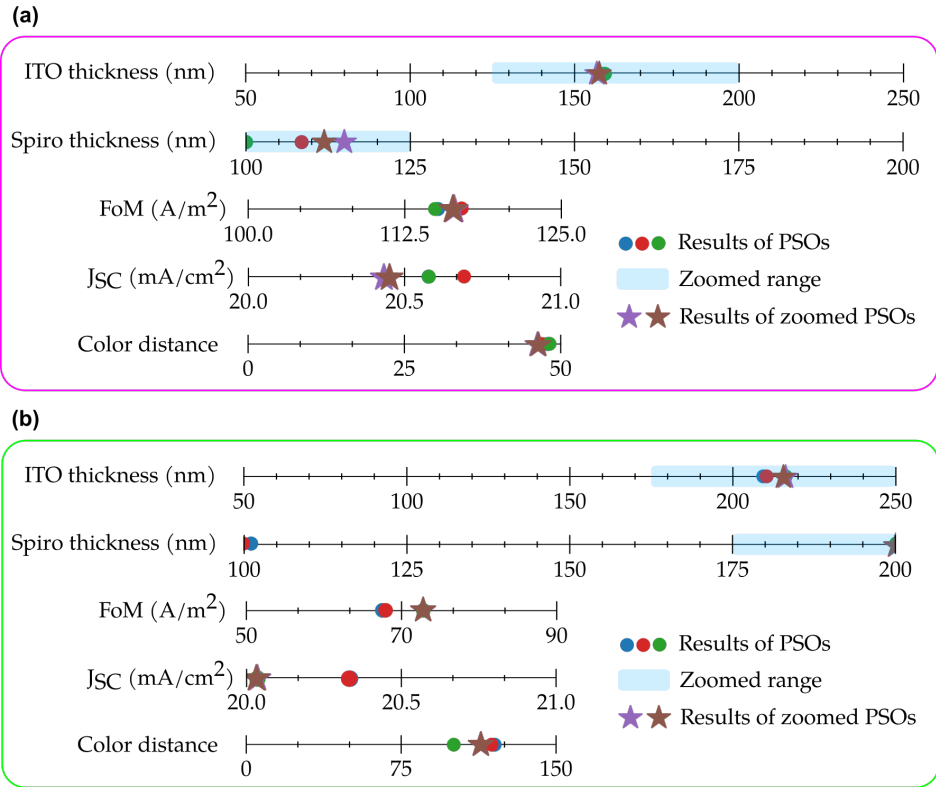
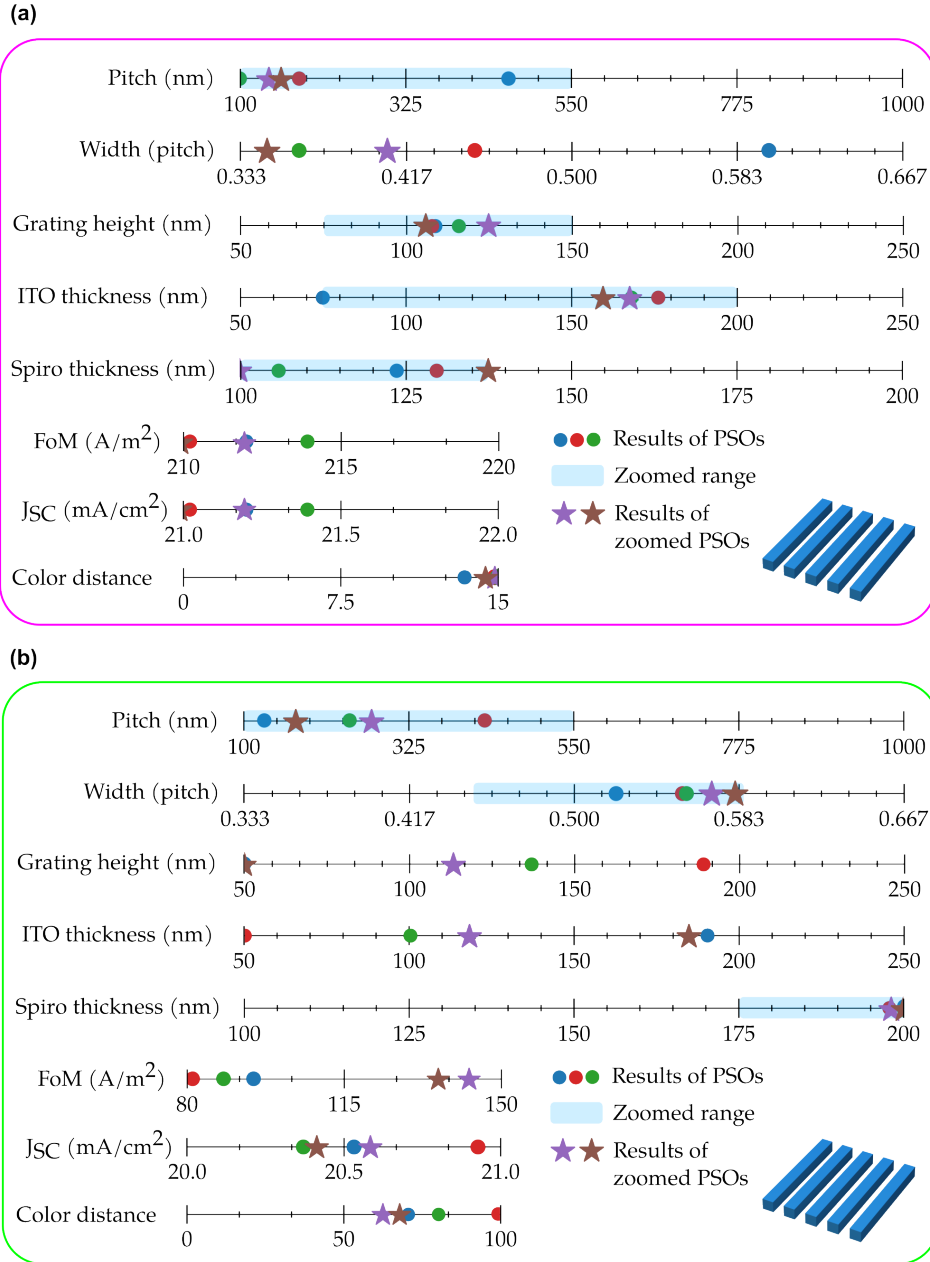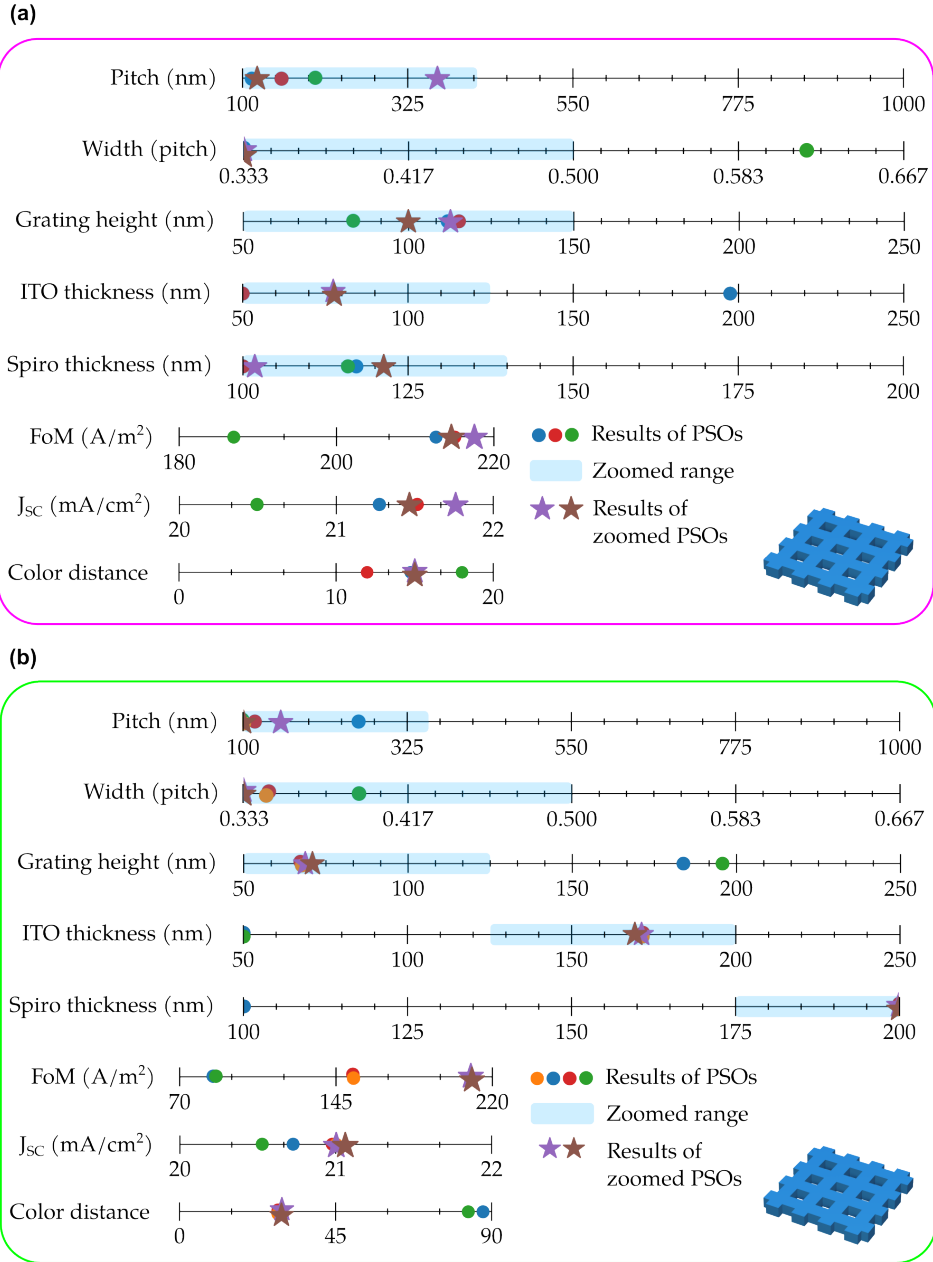**Fig. S10** Results of the Particle Swarm optimizations of planar solar cells — geometrical parameters, FoM, $J_{SC}$ and RGB distance — utilizing the Figure of Merit ($FoM_2$) defined in the main article, for (a) magenta RGB $(255, 0, 255)$ and (b) green RGB $(0, 255, 0)$. The circular marks in the parameter grids represent the results of the wide-ranged optimizations, the regions highlighted by blue correspond to the zoom intervals (new parameter amplitudes) and the star marks are the results of the zoomed PSOs.
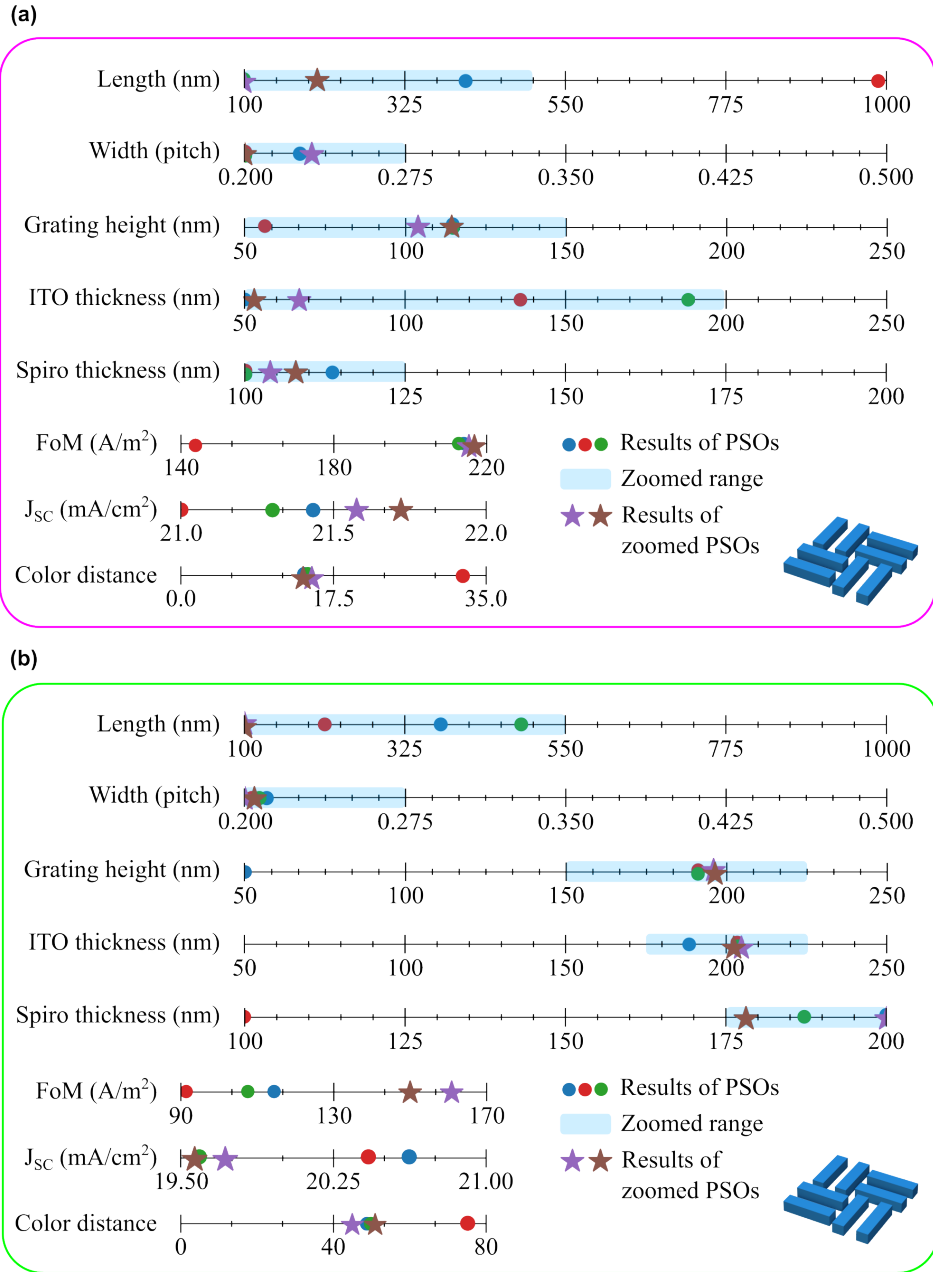
**Fig. S11** Results of the Particle Swarm optimizations of solar cells with top linear gratings — geometrical parameters, FoM, $J_{SC}$ and RGB distance — utilizing the Figure of Merit defined in the main article, for (a) magenta RGB $(255, 0, 255)$ and (b) green RGB $(0, 255, 0)$. The circular marks in the parameter grids represent the results of the wide-ranged optimizations, the regions highlighted by blue correspond to the zoom intervals (new parameter amplitudes) and the star marks are the results of the zoomed PSOs.
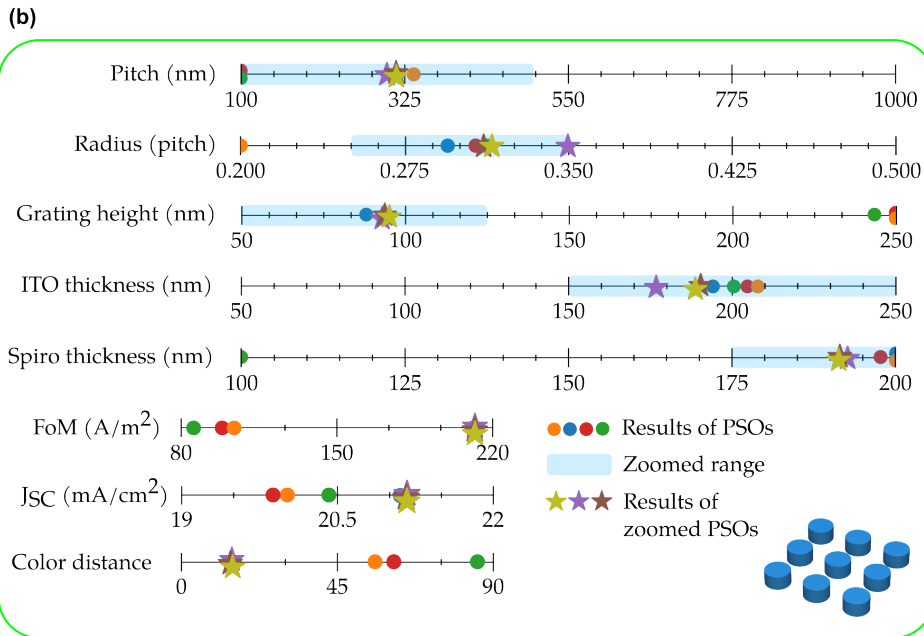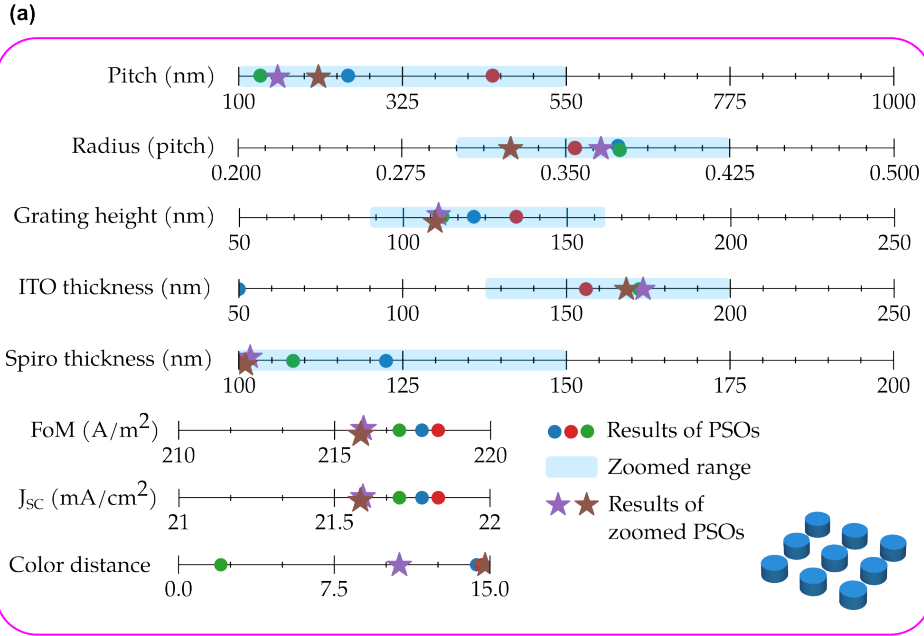
S15

**Fig. S12** Results of the Particle Swarm optimizations of solar cells with top crossed gratings — geometrical parameters, FoM, $J_{SC}$ and RGB distance — utilizing the Figure of Merit defined in the main article, for (a) magenta RGB $(255, 0, 255)$ and (b) green RGB $(0, 255, 0)$. The circular marks in the parameter grids represent the results of the wide-ranged optimizations, the regions highlighted by blue correspond to the zoom intervals (new parameter amplitudes) and the star marks are the results of the zoomed PSOs.

**Fig. S13** Results of the Particle Swarm optimizations of solar cells with checkerboards — geometrical parameters, FoM, $J_{SC}$ and RGB distance — utilizing the Figure of Merit defined in the main article, for (a) magenta RGB $(255, 0, 255)$ and (b) green RGB $(0, 255, 0)$. The circular marks in the parameter grids represent the results of the wide-ranged optimizations, the regions highlighted by blue correspond to the zoom intervals (new parameter amplitudes) and the star marks are the results of the zoomed PSOs.
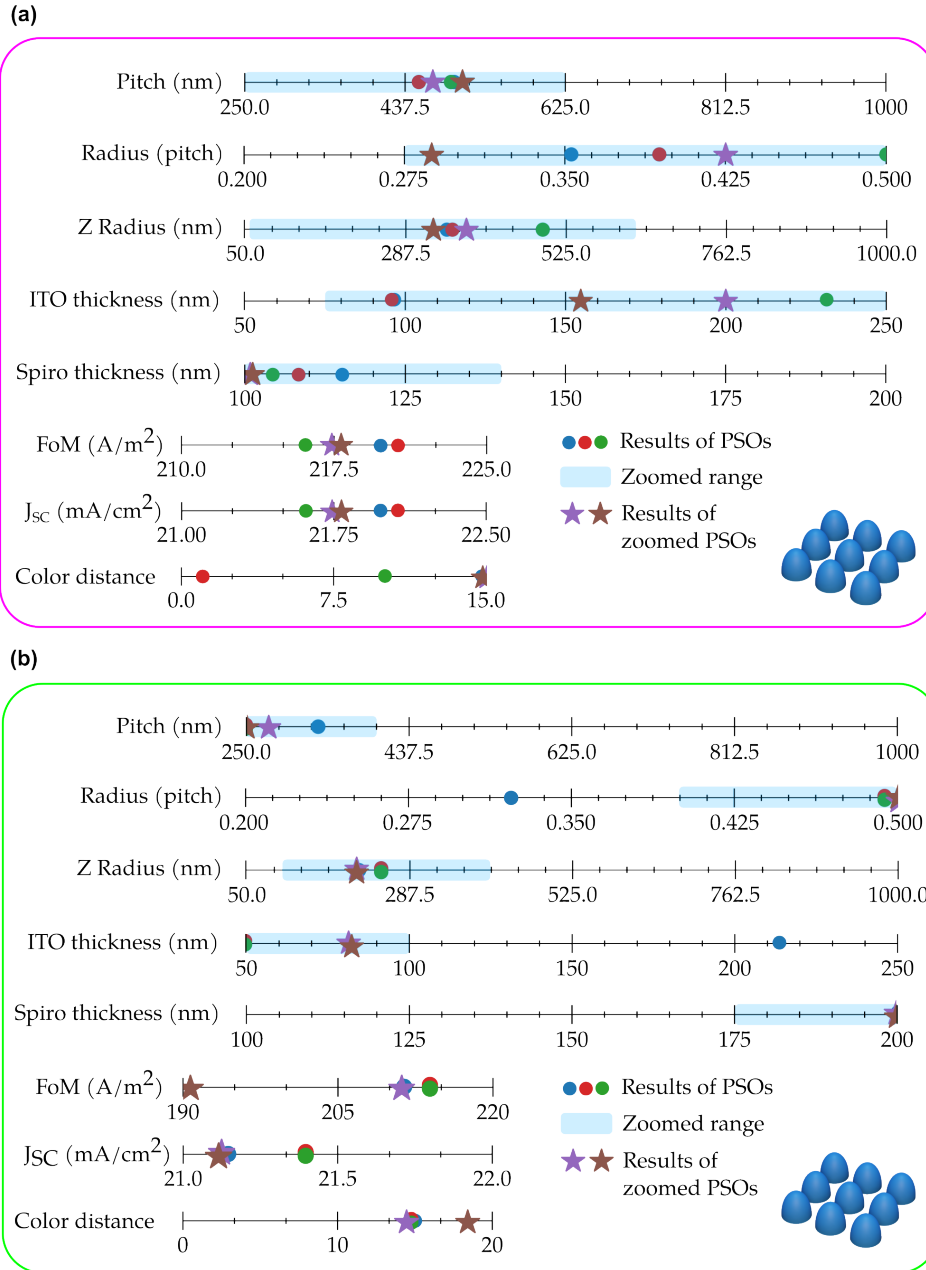
S17

**Fig. S14** Results of the Particle Swarm optimizations of solar cells with top circular nanopillars — geometrical parameters, FoM, $J_{SC}$ and RGB distance — utilizing the Figure of Merit defined in the main article, for (a) magenta RGB $(255, 0, 255)$ and (b) green RGB $(0, 255, 0)$. The circular marks in the parameter grids represent the results of the wide-ranged optimizations, the regions highlighted by blue correspond to the zoom intervals (new parameter amplitudes) and the star marks are the results of the zoomed PSOs.

S18

**Fig. S15** Results of the Particle Swarm optimizations of solar cells with top domes — geometrical parameters, FoM, $J_{SC}$ and RGB distance — utilizing the Figure of Merit defined in the main article, for (a) magenta RGB $(255, 0, 255)$ and (b) green RGB $(0, 255, 0)$. The circular marks in the parameter grids represent the results of the wide-ranged optimizations, the regions highlighted by blue correspond to the zoom intervals (new parameter amplitudes) and the star marks are the results of the zoomed PSOs.

**Table S3**  Results of the optimization of planar and structured cells, for magenta $(255, 0, 255)$ and green $(0, 255, 0)$: values of FoM, as defined by Equation (S3), $J_{SC}$ and respective RGB colours, along with the optimal geometry parameters and corresponding size accurate illustrations (considering a cell base $1\,\mu m^2$), where the thicknesses of the LT, ITO and Spiro layers are represented as h, $t_{ITO}$ and $t_{Spiro}$, respectively.
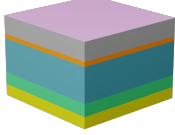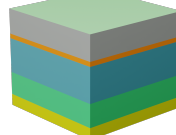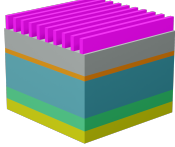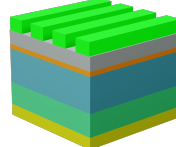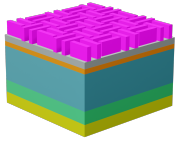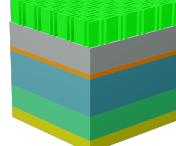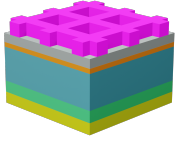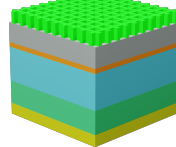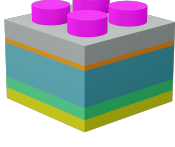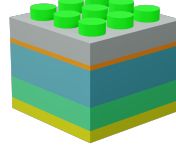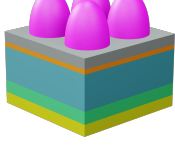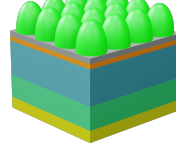
| Illustration | Geometry | Illustration | Geometry |
|---|---|---|---|
| | $t_{ITO} = 157.72\,nm$ <br> $t_{Spiro} = 108.45\,nm$ | | $t_{ITO} = 216.22\,nm$ <br> $t_{Spiro} = 200.00\,nm$ |
| | Pitch $= 100.00\,nm$ <br> Width $= 0.36$ <br> h $= 116.18\,nm$ <br> $t_{ITO} = 168.28\,nm$ <br> $t_{Spiro} = 105.84\,nm$ | | Pitch $= 275.06\,nm$ <br> Width $= 0.57$ <br> h $= 113.64\,nm$ <br> $t_{ITO} = 118.50\,nm$ <br> $t_{Spiro} = 198.13\,nm$ |
| | Length $= 202.92\,nm$ <br> Width $= 0.10$ <br> h $= 114.86\,nm$ <br> $t_{ITO} = 53.42\,nm$ <br> $t_{Spiro} = 108.34\,nm$ | | Length $= 100.00\,nm$ <br> Width $= 0.10$ <br> h $= 196.08\,nm$ <br> $t_{ITO} = 204.71\,nm$ <br> $t_{Spiro} = 200.00\,nm$ |
| | Pitch $= 365.46\,nm$ <br> Width $= 0.33$ <br> h $= 112.92\,nm$ <br> $t_{ITO} = 77.63\,nm$ <br> $t_{Spiro} = 101.78\,nm$ | | Pitch $= 100.00\,nm$ <br> Width $= 0.33$ <br> h $= 71.25\,nm$ <br> $t_{ITO} = 169.40\,nm$ <br> $t_{Spiro} = 200.00\,nm$ |
| | Pitch $= 449.36\,nm$ <br> Radius $= 0.35$ <br> h $= 134.81\,nm$ <br> $t_{ITO} = 155.95\,nm$ <br> $t_{Spiro} = 100.03\,nm$ | | Pitch $= 300.67\,nm$ <br> Radius $= 0.35$ <br> h $= 93.22\,nm$ <br> $t_{ITO} = 176.98\,nm$ <br> $t_{Spiro} = 192.56\,nm$ |
| | Pitch $= 454.97\,nm$ <br> Radius $= 0.39$ <br> Z radius $= 357.73\,nm$ <br> $t_{ITO} = 96.04\,nm$ <br> $t_{Spiro} = 108.35\,nm$ | | Pitch $= 250.00\,nm$ <br> Radius $= 0.49$ <br> Z radius $= 247.98\,nm$ <br> $t_{ITO} = 50.00\,nm$ <br> $t_{Spiro} = 200.00\,nm$ |

**Table S4** Results of the optimizations of planar and structured cells, for magenta $(255, 0, 255)$ and green $(0, 255, 0)$: values of FoM, as defined by Equation (S3), $J_{SC}$, $J_{SC}$ gain, with respect to the reference cell, and cell colours, in RGB.

| Structures | RGB colour | | FoM $(A/m^2)$ | $J_{SC}$ $(mA/cm^2)$ | $J_{SC}$ gain$(\%)$ |
|---|---|---|---|---|---|
| Planar | ● | $(255, 44, 239)$ | 117.11 | 20.69 | 0.00% |
| | ● | $(65, 255, 93)$ | 72.85 | 20.04 | -3.14% |
| Linear gratings | ● | $(246, 12, 255)$ | 213.95 | 21.40 | 3.44% |
| | ● | $(17, 255, 60)$ | 142.76* | 20.58 | -0.62% |
| Checkerboards | ● | $(241, 0, 255)$ | 217.19 | 21.72 | 4.98% |
| | ● | $(27, 255, 36)$ | 160.99* | 19.72 | -4.68% |
| Crossed gratings | ● | $(243, 9, 255)$ | 217.60 | 21.76 | 5.18% |
| | ● | $(7, 255, 29)$ | 210.62* | 21.06 | 1.79% |
| Circular nanopillars | ● | $(255, 4, 241)$ | 218.32 | 21.83 | 5.52% |
| | ● | $(13, 255, 7)$ | 211.77 | 21.18 | 2.37% |
| Domes | ● | $(254, 0, 255)$ | 220.66 | 22.07 | 6.68% |
| | ● | $(13, 255, 7)$ | 213.96 | 21.40 | 3.44% |

*Colour limit increased to 30.

## S5 Monte Carlo Simulation

The Monte Carlo method was employed as a probabilistic model that included an element of geometrical randomness in the simulation of the optimal solar cells. By performing this test, it was possible to evaluate the sensitivity of the optical properties of the solar cells to the geometrical parameters of the light-trapping structures. Figures S16(a)–(e) contain the colours of the solar cells, in the CIE Colour System gamut, after an adjustment around the optimal structural variables with a 5% margin, for 500 simulations. The corresponding RGB distances relative to the original colour were calculated for all iterations, and the respective $J_{SC}$ of the cells were attained. The analysis of the gaussian fit of the distributions of the previous quantities resulted in the standard deviation values shown in Figures S16(f), (g), for RGB distance and $J_{SC}$, respectively.

This study revealed that the divergence of the chromaticity of the cells was more significant for less compact structures: domes and circular nanopillars revealed higher standard deviation values of RGB distance, followed by linear gratings and then the most compact structures, checkerboards and crossed gratings. Regarding $J_{SC}$, the values attained for solar cells with linear gratings and with domes showed more stability, while crossed gratings and circular nanopillars originated the largest discrepancies.

According to the results of the Monte Carlo analysis, the production of solar cells with domes appears to be the most challenging and sensitive to the dimensions. The dome geometry that generates a magenta complexion in the solar cell shifted to blue and red, for a small geometric variation. Similarly, the green cell shifted to yellow and cyan. Thus, the manufacturing of these cells cannot sustain geometrical errors higher than 5%, to avoid colour inconsistencies.
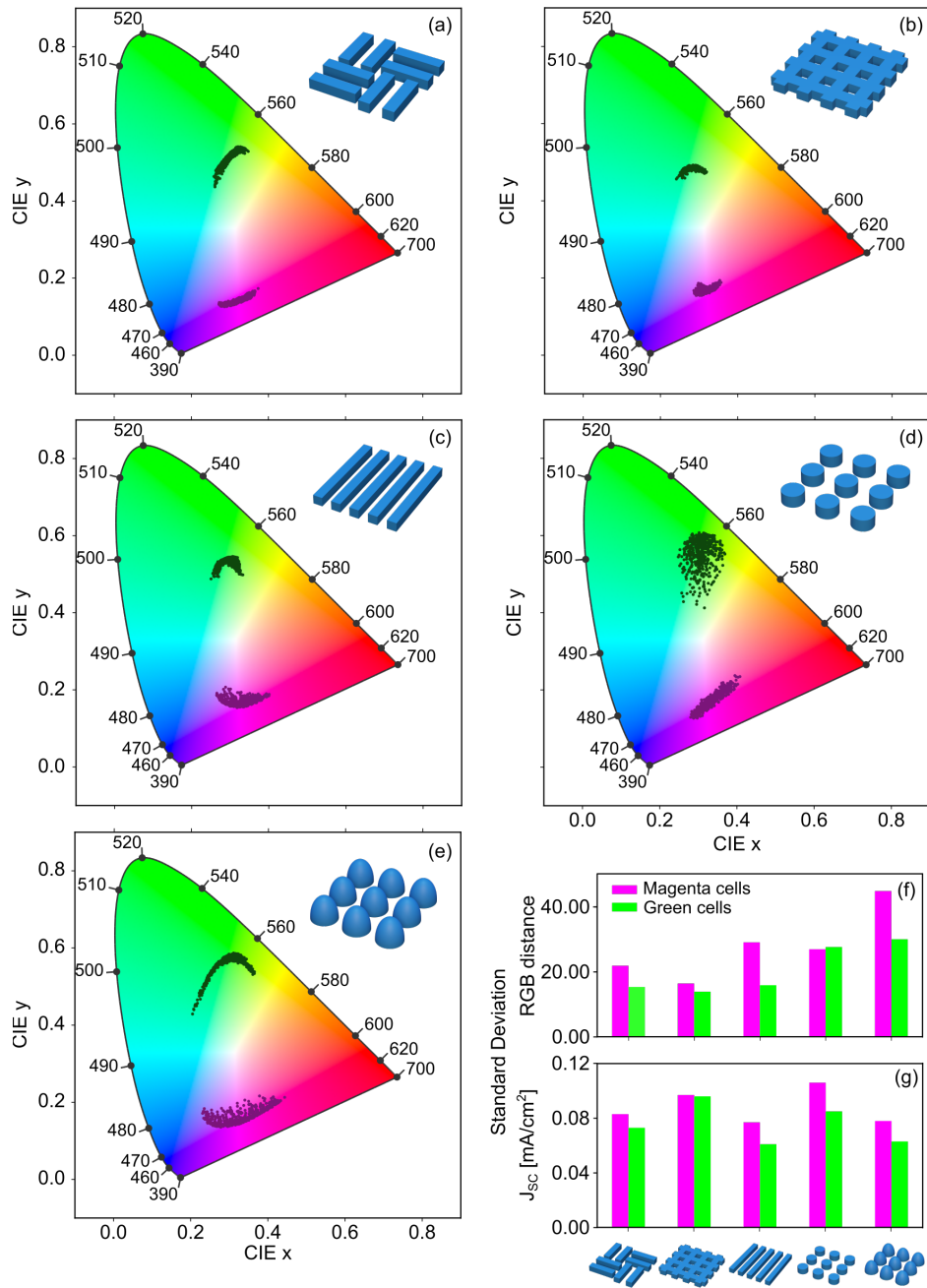
S21

**Fig. S16** (a)–(e) Chromaticity of the solar cells obtained by Monte Carlo simulation, for a simultaneous stochastic variation of the optimal LT parameters up to 5%. The top markers (in the green region of the gamut) are the results obtained for the green solar cells, while the bottom markers (in the magenta region) were obtained for the magenta cells with the light trapping structure illustrated on the top-right. (f) Standard deviation of the RGB distance of the chromaticities present in (a)–(e), relative to the original colour obtained at the optimization, and (g) standard deviation of $J_{SC}$ of the respective cells.

# References

[1] RefractiveIndex.INFO - Refractive Index Database. https://refractiveindex.info/ Accessed 2023-09-20

[2] Haque, S., Mendes, M.J., Sanchez-Sobrado, O., Águas, H., Fortunato, E., Martins, R.: Photonic structured TiO$_2$ for high-efficiency, flexible and stable perovskite solar cells. Nano Energy **59**, 91–101 (2019) https://doi.org/10.1016/J.NANOEN.2019.02.023

[3] Haque, S., Alexandre, M., Mendes, M.J., Águas, H., Fortunato, E., Martins, R.: Design of wave-optical structured substrates for ultra-thin perovskite solar cells. Applied Materials Today **20**, 100720 (2020) https://doi.org/10.1016/J.APMT.2020.100720

[4] Schuster, C.S., Crupi, I., Halme, J., Koç, M., Mendes, M.J., Peters, I.M., Yerci, S.: In: Lackner, M., Sajjadi, B., Chen, W.-Y. (eds.) Empowering Photovoltaics with Smart Light Management Technologies, pp. 1165–1248. Springer, Cham (2022). https://doi.org/10.1007/978-3-030-72579-2_112